

## Electrocatalytic Reduction of Oxygen by FePt Alloy Nanoparticles

Wei Chen,<sup>†</sup> Jaemin Kim,<sup>‡</sup> Shouheng Sun,<sup>‡</sup> and Shaowei Chen<sup>\*,†</sup>

Department of Chemistry and Biochemistry, University of California, 1156 High Street, Santa Cruz, California 95064, and Department of Chemistry, Brown University, Providence, Rhode Island 02912

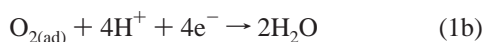
Received: November 19, 2007; In Final Form: January 2, 2008

Fe<sub>x</sub>Pt<sub>100-x</sub> nanoparticles of different compositions ( $x = 63, 58, 54, 42, 15,$  and  $0$ ) were prepared and loaded onto a glassy carbon (GC) electrode where their catalytic activities in the electroreduction of oxygen were examined and compared. Cyclic and rotating disk voltammetric studies of the resulting Fe<sub>x</sub>Pt<sub>100-x</sub>/GC electrodes showed that the catalytic activity for oxygen reduction exhibited a peak-shape dependence on the particle composition ( $x$ ). Among the series of nanocatalysts under study, Fe<sub>42</sub>Pt<sub>58</sub> particles showed the maximum activity for O<sub>2</sub> reduction in terms of the reduction overpotential and current density. This was accounted for by the effects of the Fe content on the electronic structures of the Pt active sites and the resulting Pt–O interactions. Kinetic analyses showed that direct four-electron reduction of adsorbed oxygen occurred on these catalyst surfaces. Additionally, the rate constant of O<sub>2</sub> reduction increased with increasing Pt content in the alloy particles; yet, at  $x \leq 42$ , the rate constant exhibited only a very small increment. These studies suggest that the Fe<sub>42</sub>Pt<sub>58</sub> particles might represent an optimal composition for oxygen reduction among the series of nanoparticle catalysts under the present study.

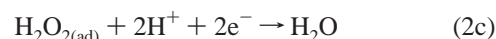
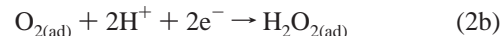
### Introduction

In recent years, fuel cells such as direct methanol fuel cells (DMFCs) and polymer electrolyte membrane fuel cells (PEMFCs) are attracting much attention due to their potential applications as effective power sources with high-energy efficiency and low air pollution.<sup>1–3</sup> To improve the performance and to reduce the costs of fuel cells, a wide variety of electrocatalysts have been prepared and evaluated for anodic and cathodic electron-transfer reactions.<sup>4–7</sup> Oxygen electroreduction represents a critical cathodic process in fuel cells. In the past decades, various cathode catalysts, such as single crystals of noble metals,<sup>8,9</sup> single crystals modified with non-noble metals,<sup>10–12</sup> Pt-free catalysts,<sup>13–22</sup> and Pt-based metal alloys, have been tested for oxygen reduction. Of these, Pt alloys (e.g., NiPt, CoPt, FePt, CrPt, etc.),<sup>23–31</sup> especially nanosized Pt alloys,<sup>25,32–34</sup> have demonstrated substantially greater activities than others. By incorporating a second metal into the Pt catalysts, the alloying process results in a favorable Pt–Pt distance for the dissociative adsorption of O<sub>2</sub> because the base transition-metal atoms are typically smaller than Pt, leading to enhanced catalytic activity for oxygen electroreduction.<sup>35,36</sup>

Oxygen reduction reactions (ORR) on the cathode surface have complicated reaction pathways.<sup>6,37</sup> The most efficient pathway is the so-called direct four-electron reduction of adsorbed oxygen to water (the subscript “ad” denotes surface adsorbed states)



Another less efficient pathway involves two steps in which oxygen is first reduced to hydrogen peroxide intermediates and then electrochemically reduced to water



Although considerable efforts have been devoted to the studies of cathode electrocatalysts, in most cases a measurable O<sub>2</sub> reduction current is detected only at potentials that are much more negative than the standard potential of +1.229 V (vs the normal hydrogen electrode, NHE). The high overpotentials arise primarily because of the sluggish electron-transfer kinetics. In recent years, numerous mechanistic studies have been carried out that are geared toward a fundamental understanding of the reaction dynamics for catalytic activity improvement and optimization.<sup>24,35,38–42</sup> It is usually believed that, in order to enhance the ORR activity of Pt-based alloy catalysts, adsorption of OH on the second metal must be facilitated, whereas the adsorption on the Pt sites should be diminished, since high coverage of adsorbed OH species on the Pt surface has been proved to inhibit the oxygen reduction reactions.<sup>8,35,39,43</sup> In previous X-ray absorption near-edge structure studies, binary alloys such as CrPt and FePt have been found to exhibit these favorable chemisorption characteristics of OH species.<sup>35</sup>

Of these, FePt bulk alloys have been studied extensively both experimentally and theoretically.<sup>23,31,35,38,40,44–46</sup> They are typically prepared by the sputtering method and exhibit higher electrocatalytic activities for ORR than the pure Pt metal<sup>23</sup> as well as other binary alloys such as NiPt, MnPt, and CoPt.<sup>23,35</sup> In these studies, the alloy composition has been found to be one of the important parameters that dictate the electrocatalytic performance.<sup>23</sup> Yet, so far no ORR studies have been carried

\* To whom correspondence should be addressed. E-mail: schen@chemistry.ucsc.edu.

<sup>†</sup> University of California, Santa Cruz.

<sup>‡</sup> Brown University.

**TABLE 1: Core Size and Elemental Composition of the Fe<sub>x</sub>Pt<sub>100-x</sub> Nanoparticles<sup>53</sup>**

core composition <sup>a</sup>	Pt	Fe <sub>15</sub> Pt <sub>85</sub>	Fe <sub>42</sub> Pt <sub>58</sub>	Fe <sub>54</sub> Pt <sub>46</sub>	Fe <sub>58</sub> Pt <sub>42</sub>	Fe <sub>63</sub> Pt <sub>37</sub>
core size (nm) <sup>b</sup>	2.78 ± 0.95	2.47 ± 0.56	2.35 ± 0.18	2.52 ± 0.81	2.48 ± 0.38	2.42 ± 0.61

<sup>a</sup> Particle core compositions were evaluated by energy-dispersive X-ray analysis. <sup>b</sup> Particle core sizes were derived from TEM measurements.

out with nanosized FePt alloy particles. It is well-known that nanoparticles exhibit a substantially higher density of active atomic steps, edges, and kinks that may result in higher catalytic activities than the bulk counterparts.<sup>47</sup> Thus, in this paper, a series of Fe<sub>x</sub>Pt<sub>100-x</sub> nanoparticles ( $x = 63, 58, 54, 42, 15,$  and 0) were prepared by a chemical reduction method and their electrocatalytic activities for ORR were examined and compared by cyclic and rotating disk voltammetry (RDV). Because of the similarity of the particle size and dispersity, the core size effects<sup>45,48-50</sup> on the catalytic activity were minimized, and the results indicated that FePt nanoparticles with the Fe/Pt atomic ratio around 1:1 appeared to exhibit the optimal composition for ORR among the series of nanoparticle catalysts in the present study.

## Experimental Section

**Materials.** Perchloric acid (HClO<sub>4</sub>, Fisher, 99.999%) was used as received. Water was supplied by a Barnstead Nanopure water system (18.3 MΩ cm). Ultrapure N<sub>2</sub> and O<sub>2</sub> were used for the deaeration of the electrolytes and oxygen reduction reaction, respectively.

**Preparation of Fe<sub>x</sub>Pt<sub>100-x</sub> Nanoparticles.** The synthesis and characterization of the Fe<sub>x</sub>Pt<sub>100-x</sub> nanoparticles stabilized by oleylamine and oleic acid have been described previously.<sup>51,52</sup> In a typical reaction, under a gentle flow of N<sub>2</sub>, Pt(acetylacetonate)<sub>2</sub>, 1,2-hexadecanediol, dioctylether were mixed at room temperature and heated to 100 °C. Oleic acid, oleyl amine, and different amounts of Fe(CO)<sub>5</sub> were added and the mixture was heated to reflux (297 °C) for 30 min. The heat source was removed, and the reaction mixture was cooled down to room temperature. The black product was precipitated by adding ethanol and separated by centrifugation. The supernatant was discarded and the black precipitate was dispersed in hexane in the presence of oleic acid and oleylamine. Then, ethanol was added to the dispersion and the suspension was centrifuged again. The precipitate was redispersed in hexane. From transmission electron microscopy (TEM) measurements, the particles were found to exhibit an average core diameter of 2–3 nm with a very narrow size distribution (a representative TEM micrograph for the Pt particles was included in the Supporting Information, Figure S1; others have been reported earlier<sup>53</sup>). The particle size and composition<sup>53</sup> were summarized in Table 1.

**Electrochemistry.** A glassy carbon (GC) disk electrode (Bioanalytical Systems, 3.0 mm in diameter) was first polished with alumina slurries (0.05 μm) and then cleaned by sonication in 0.1 M HNO<sub>3</sub>, H<sub>2</sub>SO<sub>4</sub>, and Nanopure water for 10 min successively. Eight μL of the Fe<sub>x</sub>Pt<sub>100-x</sub> nanoparticles dissolved in CH<sub>2</sub>Cl<sub>2</sub> (1.0 mg/mL) was then dropcast onto the clean GC electrode surface by a Hamilton microliter syringe (the resulting electrodes were denoted as Fe<sub>x</sub>Pt<sub>100-x</sub>/GC). The particle films were dried by a gentle nitrogen stream for 2 min. The organic protecting ligands were then removed by oxidation in an ultraviolet ozone (UVO) chamber (Jelight Company, Inc., Model 42) for about 15 min (the effectiveness of UVO removal of the organic layers was demonstrated by voltammetric measurements in Figure S2).<sup>52-54</sup> The particle film was then rinsed with excessive ethanol and nanopure water to remove loosely bound

particles and remaining organic deposits before being immersed into an electrolyte solution for electrochemical studies. All electrochemical experiments were performed in a single-compartment glass cell using a standard three-electrode configuration. A Ag/AgCl (in 3 M NaCl, aq) (Bioanalytical Systems, MF-2052) and a Pt coil were used as the reference and counter electrodes, respectively. All electrode potentials in the present study were referred to this Ag/AgCl reference electrode. Cyclic voltammetry (CV) and RDV were carried out by using a computer-controlled Bioanalytical Systems (BAS) Electrochemical Analyzer (Model 100B). Oxygen reduction reactions were examined by first bubbling the electrolyte solution with ultrahigh purity oxygen for at least 15 min and then blanketing the solution with an oxygen atmosphere during the entire experimental procedure. All electrochemical experiments were carried out at room temperature.

## Results and Discussion

**Cyclic Voltammetry.** Figure 1 shows the cyclic voltammograms of the Fe<sub>x</sub>Pt<sub>100-x</sub>/GC electrodes ( $x = 63, 58, 54, 42, 15,$  and 0) in 0.1 M HClO<sub>4</sub> deaerated by ultrahigh purity nitrogen. The voltammetric features are all very similar to those of a polycrystalline Pt electrode:<sup>55,56</sup> the adsorption and desorption of hydrogen within the potential range of -0.25 to 0.0 V, the double-layer capacitance region between 0.0 and +0.7 V, the formation of Pt oxides at potentials more positive than +0.7 V, and the reduction of Pt oxides in the cathodic potential scan. Such voltammetric features have been observed with other Pt-based alloys such as CoPt, NiPt, and FePt, and they are ascribed to the formation of a “Pt skin” on the catalyst surface.<sup>23-25,52-54,57,58</sup> This Pt surface enrichment is caused by Pt dissolution from the alloys and then redeposition and rearrangement on the catalyst surface during potential cycling in acidic electrolytes. From these voltammetric measurements (Figure 1), the active (Pt) surface areas were then quantitatively evaluated on the basis of the charge for the oxidation of surface-adsorbed hydrogen by assuming that hydrogen desorption yields 210 μC per cm<sup>2</sup> of the Pt surface area. Table 2 summarizes the surface areas of the six Fe<sub>x</sub>Pt<sub>100-x</sub>/GC electrodes. It can be seen that the effective (Pt) surface area increases with increasing Pt content in the particles, suggesting the formation of a thicker/larger Pt skin on particles with a higher Pt concentration.

Note that although the Pt alloys display voltammetric features consistent with those of (polycrystalline) Pt, the catalytic properties of the Pt skins might differ drastically from those of a pure Pt surface, which has been ascribed to the electronic effect of the intermetallic bonding of the base metal-rich inner layers with the surface Pt atoms.<sup>24,25,31,59,60</sup>

Figure 2 shows the cyclic voltammograms for the Fe<sub>x</sub>Pt<sub>100-x</sub>/GC electrodes in an O<sub>2</sub> saturated 0.1 M HClO<sub>4</sub> aqueous solution at the potential scan rate of 0.1 V/s. Note that the currents have been normalized to the effective Pt surface areas estimated from Figure 1 (Table 2). The observed cathodic current is ascribed to O<sub>2</sub> reduction on the particle surfaces since the GC substrate is electrochemically inert to O<sub>2</sub> reduction. The peak current density increases linearly with the square root of potential scan rate (not shown), suggesting that the O<sub>2</sub> reduction is under diffusion control. It can be seen from Figure 2 that the current

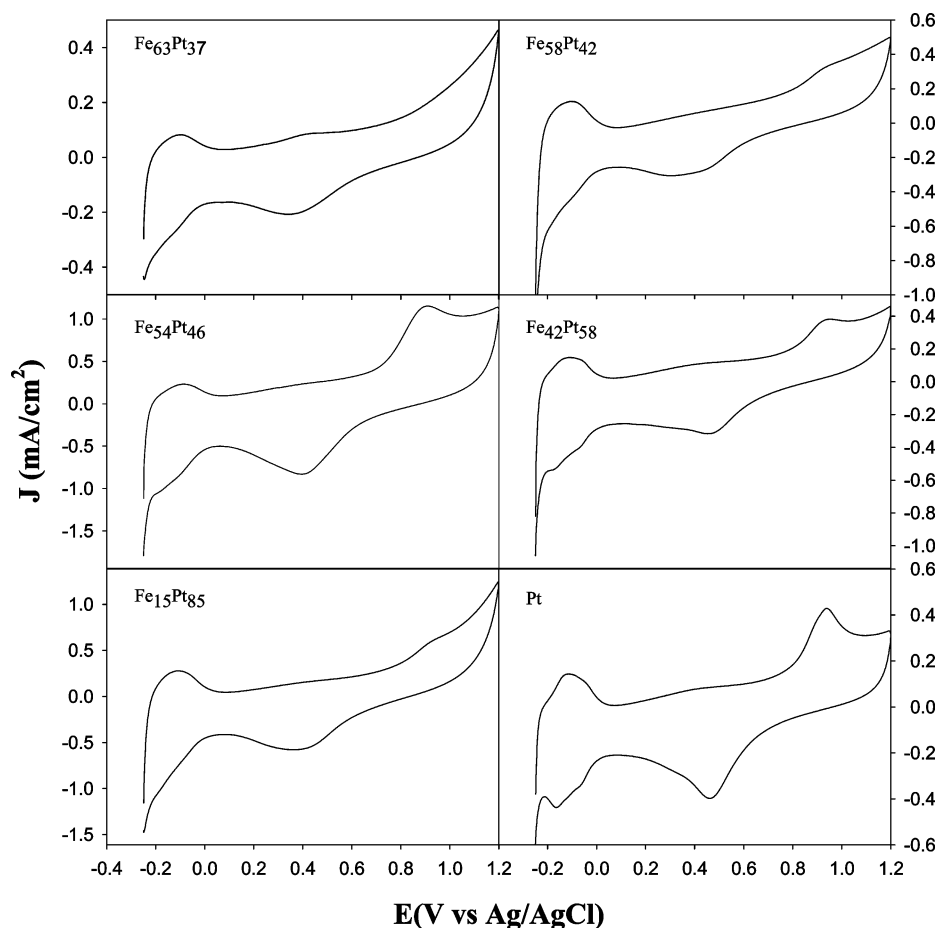


**Figure 1.** Cyclic voltammograms of the  $\text{Fe}_x\text{Pt}_{100-x}/\text{GC}$  electrodes ( $x = 63, 58, 54, 42, 15,$  and  $0$ ) after UVO treatment in  $0.1 \text{ M HClO}_4$ . The electrolyte solution was deaerated by ultrahigh-purity nitrogen for 15 min and protected by a nitrogen atmosphere during the entire experimental procedure. Current density was calculated by normalizing the voltammetric currents to the surface area of the glassy carbon electrode. Potential scan rate was  $0.1 \text{ V/s}$ .

**TABLE 2: Kinetic Parameters for  $\text{O}_2$  Reduction at  $\text{Fe}_x\text{Pt}_{100-x}$  Nanoparticle-Functionalized GC Electrodes**

$\text{Fe}_x\text{Pt}_{100-x}$	$\text{Fe}_{63}\text{Pt}_{37}$	$\text{Fe}_{58}\text{Pt}_{42}$	$\text{Fe}_{54}\text{Pt}_{46}$	$\text{Fe}_{42}\text{Pt}_{58}$	$\text{Fe}_{15}\text{Pt}_{85}$	Pt
Pt surface area ( $\text{cm}^2$ ) <sup>a</sup>	0.016	0.026	0.034	0.037	0.040	0.051
ORR onset potential (V vs Ag/AgCl) <sup>b</sup>	0.49	0.50	0.56	0.61	0.57	0.46
no. electron transfer ( $n$ ) <sup>c</sup>	3.69	4.06	3.60	3.60	3.83	3.90
reaction rate constant at $+0.32 \text{ V}$ ( $k$ , $\text{cm/s}$ ) <sup>d</sup>	$3.70 \times 10^{-3}$	$1.47 \times 10^{-3}$	$0.90 \times 10^{-3}$	$6.92 \times 10^{-3}$	$6.93 \times 10^{-3}$	$7.53 \times 10^{-3}$

<sup>a</sup> On the basis of the charge for the oxidation of hydrogen adsorbed onto the Pt surfaces (Figure 1). <sup>b</sup> Estimated from Figures 2 and 6. <sup>c</sup> The numbers of electron transferred for ORR were calculated from eq 4b. <sup>d</sup> The reaction rate constants were derived by using eq 4c.

density and onset potential of  $\text{O}_2$  reduction vary with the composition of the particles. For instance, for the pure Pt nanoparticles, the onset potential for  $\text{O}_2$  reduction is about  $+0.46 \text{ V}$ , and a current peak can be observed at  $-0.035 \text{ V}$ ; whereas for  $\text{Fe}_{42}\text{Pt}_{58}$ , the onset potential shifts positively to  $+0.61 \text{ V}$ , and a peak appears at ca.  $+0.23 \text{ V}$ . Results for other particles fall in the intermediate range (Table 2). These observations suggest that the FePt nanoalloy catalysts with a “Pt-skin” actually behave more favorably in oxygen reduction than the pure Pt particles. For comparison, by using PdPt alloy particles,<sup>61</sup> He and Crooks observed a similar variation of the onset potential with the elemental composition of the nanoparticles, which ranged from ca.  $+0.45$  to  $+0.65 \text{ V}$  (vs Ag/AgCl); and the most positive onset potential was found with the Pt-rich  $\text{Pd}_{17}\text{Pt}_{83}$  particles. In contrast, in another study using ordered arrays of Pt and CoPt nanoparticles,<sup>62</sup> Kumar and Zou found that the ORR onset potentials remained virtually invariant at  $+0.45 \text{ V}$  (vs Ag/AgCl), regardless of the particle elemental composition. The

discrepancy most likely arises from the different structures of the nanoparticle catalysts that are prepared by different synthetic protocols.

The compositional effects of the  $\text{Fe}_x\text{Pt}_{100-x}$  nanoparticles on the catalytic activity can be further illustrated by the ORR peak current density, which is summarized in Figure 3. It can be seen that the  $\text{O}_2$  reduction current density first increases and then decreases with the Pt content in  $\text{Fe}_x\text{Pt}_{100-x}$  nanoparticles; and the FePt particles with the Fe:Pt atomic ratio around 1:1 exhibit the largest current density for  $\text{O}_2$  reduction. For instance, for the  $\text{Fe}_{54}\text{Pt}_{46}$  and  $\text{Fe}_{42}\text{Pt}_{58}$  particles, the peak current density is  $2.97$  and  $3.15 \text{ mA/cm}^2$ , respectively; whereas it decreases markedly to  $0.60 \text{ mA/cm}^2$  for the  $\text{Fe}_{63}\text{Pt}_{37}$  particles and  $0.85 \text{ mA/cm}^2$  for the Pt particles. This is in good agreement with previous studies of  $\text{O}_2$  reduction on FePt bulk alloys prepared by the sputtering method<sup>23</sup> but is markedly different from the observation with PdPt alloy nanoparticles,<sup>61</sup> where the maximum activity for ORR occurs at a Pd:Pt ratio of 1:5. It has been

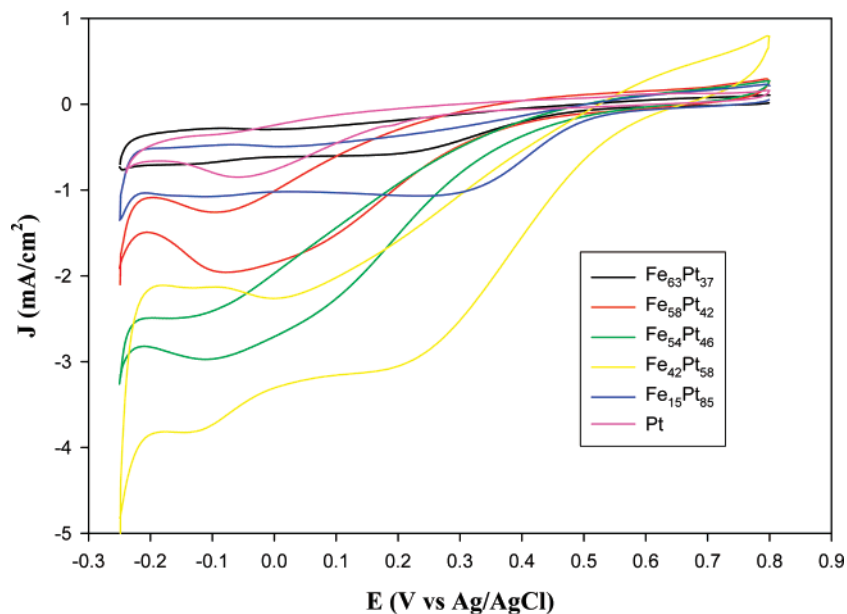


**Figure 2.** Cyclic voltammograms of the  $\text{Fe}_x\text{Pt}_{100-x}/\text{GC}$  electrodes (same as those in Figure 1) in 0.1 M  $\text{HClO}_4$  saturated with oxygen. Current density was calculated by normalizing the voltammetric currents to the effective platinum surface areas which were estimated from Figure 1. Potential scan rate was 0.1 V/s.

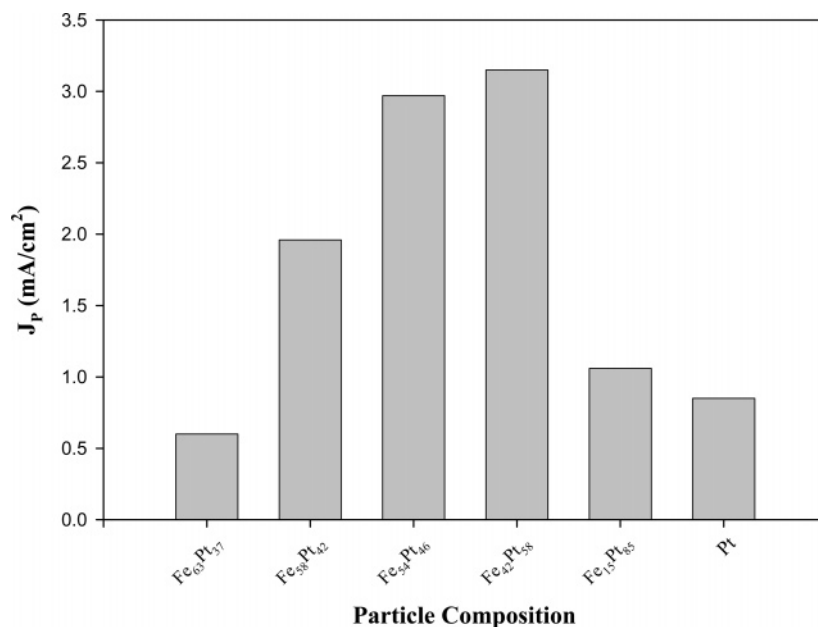


**Figure 3.** Peak current density of  $\text{O}_2$  reduction as a function of the  $\text{Fe}_x\text{Pt}_{100-x}$  nanoparticle composition. Data were obtained from Figure 2.

proposed that the addition of an early transition metal (M) to Pt changes the geometric (Pt–Pt bond distance and coordination number) and/or electronic structures (Pt–OH bond energy) of Pt.<sup>24,27</sup> Consequently, for M–Pt catalysts, the catalytic properties for ORR are strongly dependent on the type and concentration of M in the (sub)surface atomic layers.

**Rotating Disk Voltammetry.** To further examine the electrocatalytic activity, the kinetics of oxygen reduction at the  $\text{Fe}_x\text{Pt}_{100-x}$  nanoparticles was also examined as a function of the catalyst composition by RDV. The rotating disk electrodes (RDEs) were the same as those used in the cyclic voltammetric studies (Figures 1 and 2). Figures 4A and 5A show a series of RDE voltammograms of oxygen reduction at the Pt/GC and  $\text{Fe}_{42}\text{Pt}_{58}/\text{GC}$  electrodes, respectively, at different rotation rates in a 0.1 M  $\text{HClO}_4$  solution saturated with  $\text{O}_2$  (DC ramp 20 mV/s). Additional data for the other electrodes were included in the Supporting Information (Figures S3–S6). Again, the currents

were all normalized to the effective Pt surface areas as summarized in Table 2. Note that, between +0.30 and +0.55 V, the cathodic currents were under mixed kinetic diffusion control, and at more negative potentials, the oxygen reduction was limited by diffusion, as reflected by the linearity of the Koutecky–Levich plots in Figures 4B and 5B. On both electrodes (Figure 4A and 5A), the currents in the hydrogen adsorption/desorption potential region (i.e., below  $-0.05$  V) exhibited a slight decrease with increasingly negative potential. Similar results have also been observed previously with Pt single crystal and Pt alloy electrodes,<sup>25,63</sup> which are ascribed to the blocking of the Pt sites by hydrogen adsorption leading to impeded dissociation of the O–O bond and hence peroxide production (i.e., incomplete reduction of oxygen, eq 2b).

Additionally, at the same electrode potentials and rotation rates, the current density is the largest with the  $\text{Fe}_{42}\text{Pt}_{58}/\text{GC}$  electrode among the series of electrocatalysts under study. Figure

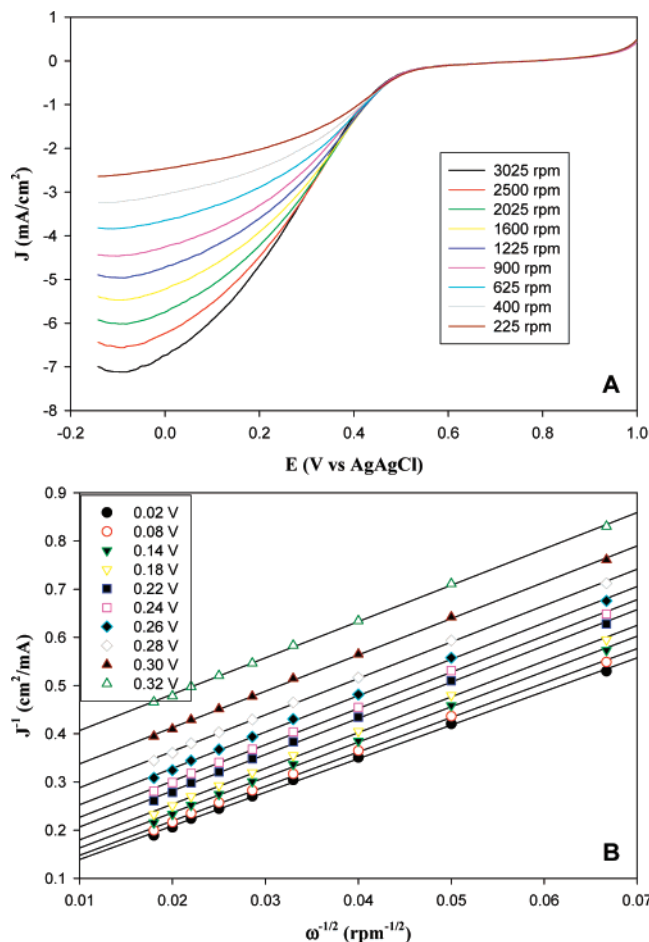
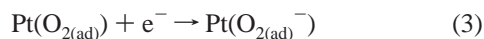


**Figure 4.** (A) RDE voltammograms for the Pt/GC electrode in oxygen-saturated 0.1 M HClO<sub>4</sub> aqueous solution at different rotation rates (shown as figure legends). Current density was calculated by normalizing the voltammetric currents to the effective platinum surface areas which were estimated from Figure 1. DC ramp 20 mV/s. (B) The corresponding Koutecky–Levich plots ( $J^{-1}$  vs  $\omega^{-0.5}$ ) at different electrode potentials. Lines are the linear regressions.

6 depicts the representative RDE voltammograms (at 1600 rpm) for the six electrodes. For instance, at the electrode potential of +0.20 V, the current density for the six electrodes was  $-0.56$  mA/cm<sup>2</sup> (Fe<sub>63</sub>Pt<sub>37</sub>),  $-1.84$  mA/cm<sup>2</sup> (Fe<sub>58</sub>Pt<sub>42</sub>),  $-2.20$  mA/cm<sup>2</sup> (Fe<sub>54</sub>Pt<sub>46</sub>),  $-3.91$  mA/cm<sup>2</sup> (Fe<sub>42</sub>Pt<sub>58</sub>),  $-3.55$  mA/cm<sup>2</sup> (Fe<sub>15</sub>Pt<sub>85</sub>), and  $-1.64$  mA/cm<sup>2</sup> (Pt), respectively. Overall, the variation of the current density with the particle composition is very similar to that observed voltammetrically (Figure 3). The same conclusion can be reached by further comparison of the onset potential (Figure 6 and Table 2) where the Fe<sub>42</sub>Pt<sub>58</sub> particles again exhibit the most positive onset potential for ORR.

It should be noted that the compositional effect on the catalytic performance as observed in the above voltammetric and RDE measurements can be rationalized by the oxygen reduction mechanism. In this, the first electron-transfer process for the adsorbed oxygen molecules represents the rate-determining step<sup>23,25</sup>



For FePt nanoparticles, O<sub>2</sub> is adsorbed onto the Pt surface sites in a linear or bridge-bonded configuration, where electrons are donated from the filled O<sub>2</sub> orbitals to the empty orbitals of Pt surface atoms by  $\sigma$  overlap. At the same time, Pt back-donates electrons from the filled d orbitals to the empty O<sub>2</sub> antibonding

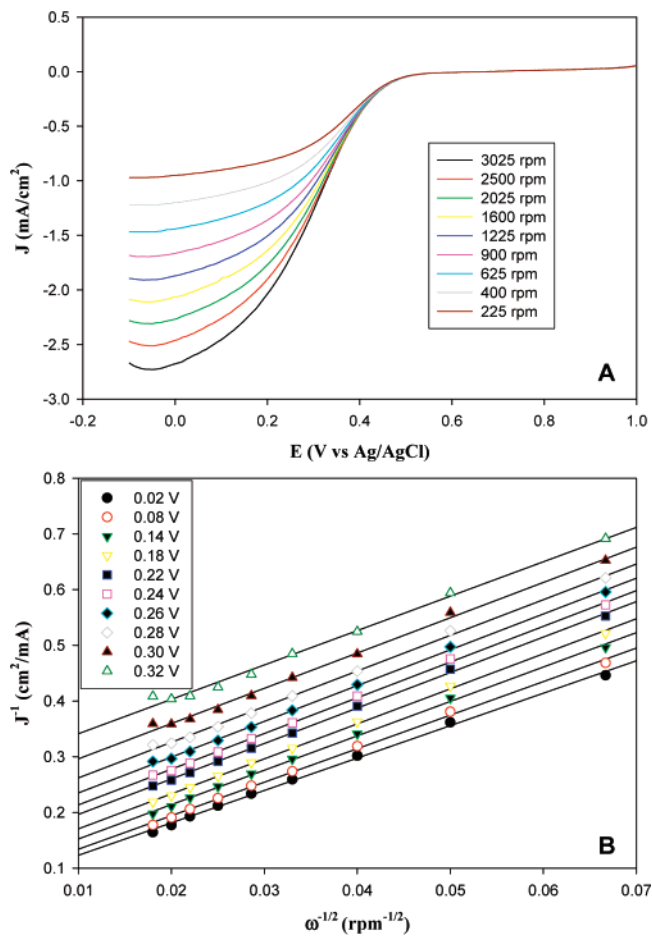


**Figure 5.** (A) RDE voltammograms for the Fe<sub>42</sub>Pt<sub>58</sub>/GC electrode in oxygen-saturated 0.1 M HClO<sub>4</sub> aqueous solution at different rotation rates (shown as figure legends). Current density was calculated by normalizing the voltammetric currents to the effective platinum surface areas, which were estimated from Figure 1. DC ramp 20 mV/s. (B) The corresponding Koutecky–Levich plots ( $J^{-1}$  vs  $\omega^{-0.5}$ ) at different electrode potentials. Lines are the linear regressions.

orbitals ( $\pi^*$ ). That is, O<sub>2</sub> is adsorbed onto the Pt surface by strong  $\sigma$ - and  $\pi$ -bonding interactions. Previous studies<sup>23,35</sup> have showed that Pt alloys by the addition of a second metal (e.g., Fe, Co, Ni, etc.) exhibit an increase of the surface d-vacancy, which facilitates electron donation from O<sub>2</sub> to surface Pt and hence strong interactions between Pt and O<sub>2</sub>. The resulting enhancement of oxygen adsorption and weakening of the O–O bond lead to fast scission of the bond and consequently enhanced ORR activities. However, with increasing Fe content in the FePt nanoparticles, excessive d-vacancy might actually diminish the back-donation of electrons from Pt to oxygen and thus reduce the activity for ORR.<sup>23</sup> As a result, too much or too little Fe in the alloy particles will weaken the ORR catalytic activity, i.e., the ORR current is anticipated to exhibit peak-shape dependence on the particle composition as observed above (e.g., Figure 3).

Moreover, in comparison with previous ORR studies using FePt bulk alloys, the nanoparticles in the present studies exhibit much larger current density. For example, at the rotation rate of 1600 rpm, the limiting current density was about  $-3.0$  mA/cm<sup>2</sup> with bulk alloys,<sup>23</sup> whereas it was ca.  $-5.4$  mA/cm<sup>2</sup> for the Fe<sub>42</sub>Pt<sub>58</sub> particles (Figure 5A).

Further insights into the ORR dynamics were then obtained from the analyses of the Koutecky–Levich plots ( $J^{-1}$  vs  $\omega^{-1/2}$ ). Figures 4B and 5B depict some representative plots at various electrode potentials for the Pt/GC and Fe<sub>42</sub>Pt<sub>58</sub>/GC electrodes, respectively (again, additional data for other electrodes were

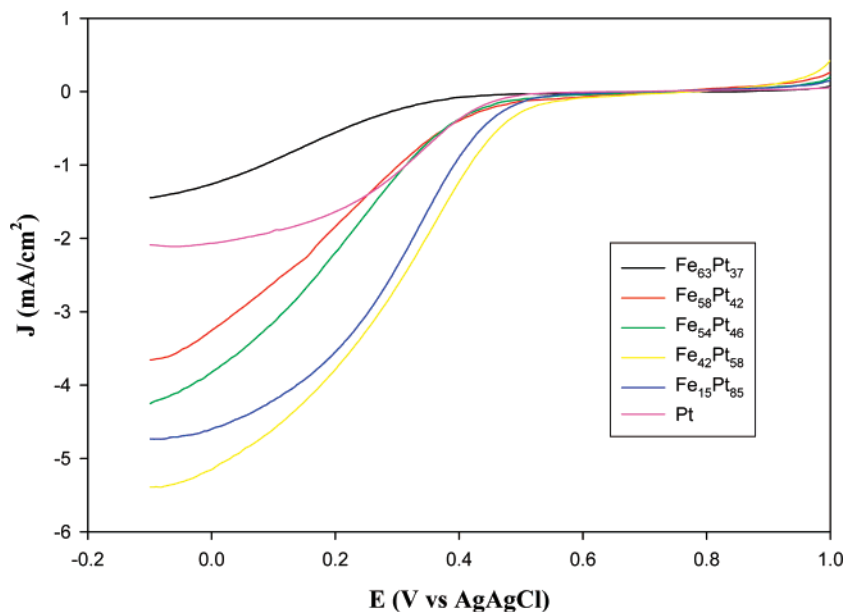


**Figure 6.** Representative RDE voltammograms of the six electrodes in oxygen-saturated 0.1 M HClO<sub>4</sub> aqueous solution. Rotation rate was 1600 rpm, and DC ramp was 20 mV/s. Other experimental conditions were the same as those in Figure 2.

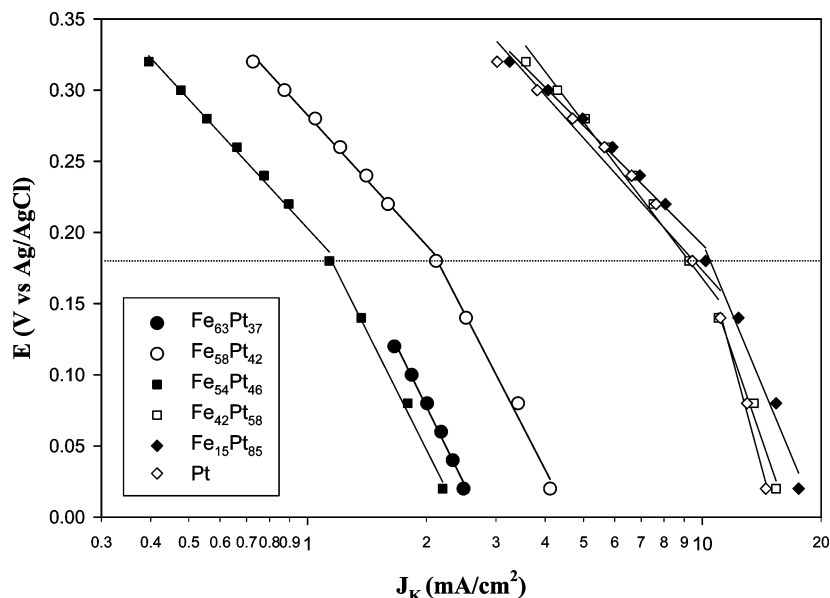


**Figure 7.** Tafel plots of the kinetic-limiting current density ( $J_K$ ) for the six electrodes. Symbols are experimental data obtained from the linear regressions of the Koutecky–Levich plots as exemplified in Figures 4B and 5B. Lines are the corresponding linear regressions. Horizontal dotted line denotes the transition potential separating the two linear regions of different slopes.

included in the Supporting Information, Figures S3 – S6). It can be seen that the slopes of the linear regressions remain approximately constant over the potential range of +0.02 to +0.32 V, indicating consistent numbers of electron transfer for ORR at different electrode potentials. The linearity and parallelism of the plots are usually taken as a strong indication of a first-order reaction with respect to dissolved O<sub>2</sub>, where the observed current can be expressed as

$$\frac{1}{J} = \frac{1}{J_K} + \frac{1}{J_D} = \frac{1}{J_K} + \frac{1}{B\omega^{1/2}} \quad (4a)$$

$$B = 0.62nFC_0D_O^{2/3}\nu^{-1/6} \quad (4b)$$

$$J_K = nFkC_O \quad (4c)$$

where  $J$  is the measured current density,  $J_K$  and  $J_D$  are the kinetic-

and diffusion limiting current density, respectively,  $\omega$  is the electrode rotation rate,  $n$  is the overall number of electron transfer,  $F$  is the Faraday constant,  $C_O$  is the bulk concentration of O<sub>2</sub> dissolved in the electrolyte,  $D_O$  is the diffusion coefficient for O<sub>2</sub>, and  $\nu$  is the kinematic viscosity of the electrolyte. So the plots of  $J^{-1}$  vs  $\omega^{-1/2}$  are anticipated to yield straight lines with the intercept corresponding to  $J_K$  (eq 4c) and the slopes reflecting the so-called  $B$  factors (eq 4b). From the latter, the numbers of electron transfer for ORR can then be estimated, by using the literature data for  $C_O = 1.26 \times 10^{-3}$  M,<sup>64</sup>  $D_O = 1.93 \times 10^{-5}$  cm<sup>2</sup>/s, and  $\nu = 1.009 \times 10^{-2}$  cm<sup>2</sup>/s.<sup>65,66</sup> Table 2 summarizes the results for the six electrodes where the number of electron transfer was all close to 4, suggesting that oxygen reduction on the Fe<sub>x</sub>Pt<sub>100-x</sub> nanoparticle surface proceed by the efficient four-electron reaction pathway (eq 1).

From the  $y$ -axis intercepts of the linear regressions of the Koutecky–Levich plots (Figures 4B and 5B), the kinetic-

limiting current density ( $J_K$ ) can be quantitatively evaluated. Figure 7 shows the corresponding Tafel plots for the six electrodes, where the overall shape is clearly similar despite the different elemental composition of the nanoparticle catalysts. This again implies that the oxygen reduction follows the same mechanism on these six different electrocatalysts. Additionally, in each Tafel plot, there exist two linear regions with distinctly different slopes, with a transition potential at ca. +0.18 V. Such a variation of the slope in the Tafel plot has been attributable to the variation of the adsorption (surface coverage) of the reaction intermediates ( $\text{OH}_{\text{ad}}$ ) and specifically adsorbed electrolyte anions with electrode potentials that consequently affects the adsorption of the  $\text{O}_2$  molecules.<sup>23,24,61</sup>

Additionally, on the basis of eq 4c, the reaction rate constants ( $k$ ) can be assessed in a quantitative fashion. Table 2 lists the ORR rate constants at the different  $\text{Fe}_x\text{Pt}_{100-x}/\text{GC}$  electrodes (at +0.32 V vs Ag/AgCl), which are all of the order of  $10^{-3}$  cm/s, very comparable to the values observed with other catalysts such as Pt–NbPO<sub>x</sub> supported on multiwalled carbon nanotubes,<sup>67</sup> and quinone-<sup>68</sup> or anthraquinone-modified<sup>69</sup> GC electrodes. Additionally, it can be seen that the ORR rate constant increases with increasing Pt content in the  $\text{Fe}_x\text{Pt}_{100-x}$  nanocatalysts with a drastic jump at  $x = 42$ , and at higher Pt contents, the increment becomes very small. Such a distinction is also manifested in Figure 7 where the Tafel plots are essentially divided into two groups. At the same electrode potentials, the kinetic currents at  $x \leq 42$  ( $\text{Fe}_{42}\text{Pt}_{58}$ ,  $\text{Fe}_{15}\text{Pt}_{85}$ , and Pt) are substantially greater than those at  $x \geq 54$  ( $\text{Fe}_{63}\text{Pt}_{37}$ ,  $\text{Fe}_{58}\text{Pt}_{42}$ , and  $\text{Fe}_{54}\text{Pt}_{46}$ ), again, signifying that the  $\text{Fe}_{42}\text{Pt}_{58}$  particles may represent the optimal composition for ORR catalysis among the series of electrocatalysts under study.

## Conclusions

The catalytic activities of the  $\text{Fe}_x\text{Pt}_{100-x}$  nanoparticles for oxygen reduction were examined and compared by using CV and RDV in an acidic electrolyte. It was found that the formation of a “Pt skin” on the alloy particle surface rendered them effective ORR catalysts as compared to the pure Pt particles. In addition, the catalytic activity for oxygen reduction was strongly dependent on the composition of the  $\text{Fe}_x\text{Pt}_{100-x}$  particles. Among the series of catalysts in the present study,  $\text{Fe}_{42}\text{Pt}_{58}$  particles exhibited the best performance for  $\text{O}_2$  reduction with the most positive onset potential and maximum reduction current density. The variation of the ORR activity with particle composition was explained by the influence of the Fe content on the electronic structure of Pt active sites and consequently the Pt–O bonding interactions. The direct four-electron reduction of adsorbed oxygen was derived from the kinetic studies using the rotating disk electrode technique. The reaction rate constant of  $\text{O}_2$  reduction on  $\text{Fe}_x\text{Pt}_{100-x}$  alloy nanoparticles was found to exhibit a drastic increase when  $x$  decreased to 42, and further increase of the Pt content in the nanoparticle electrocatalysts only led to a very small increment. These studies suggest that the  $\text{Fe}_{42}\text{Pt}_{58}$  particles might represent an optimal composition among the series of nanoparticle catalysts under the present study for oxygen reduction.

**Acknowledgment.** This work was supported in part by the National Science Foundation (CHE-0456130, CHE-0718170, and DMR-0606264).

**Supporting Information Available:** Representative TEM micrograph, additional RDE voltammograms, and Koutecky–

Levich plots. This information is available free of charge on the Internet at <http://pubs.acs.org>.

## References and Notes

- Wasmus, S.; Kuver, A. *J. Electroanal. Chem.* **1999**, *461*, 14–31.
- Lemons, R. A. *J. Power Sources* **1990**, *29*, 251–264.
- Steele, B. C. H.; Heinzl, A. *Nature* **2001**, *414*, 345–352.
- Parsons, R.; Vandermoot, T. *J. Electroanal. Chem.* **1988**, *257*, 9–45.
- Cameron, D.; Holliday, R.; Thompson, D. *J. Power Sources* **2003**, *118*, 298–303.
- Markovic, N. M.; Ross, P. N. *Surf. Sci. Rep.* **2002**, *45*, 121–229.
- Zhang, J.; Sasaki, K.; Sutter, E.; Adzic, R. R. *Science* **2007**, *315*, 220–222.
- Wang, J. X.; Markovic, N. M.; Adzic, R. R. *J. Phys. Chem. B* **2004**, *108*, 4127–4133.
- Inoue, H.; Brankovic, S. R.; Wang, J. X.; Adzic, R. R. *Electrochim. Acta* **2002**, *47*, 3777–3785.
- Zhang, J.; Mo, Y.; Vukmirovic, M. B.; Klie, R.; Sasaki, K.; Adzic, R. R. *J. Phys. Chem. B* **2004**, *108*, 10955–10964.
- Shao, M. H.; Huang, T.; Liu, P.; Zhang, J.; Sasaki, K.; Vukmirovic, M. B.; Adzic, R. R. *Langmuir* **2006**, *22*, 10409–10415.
- Mukerjee, S.; Srinivasan, S. *J. Electroanal. Chem.* **1993**, *357*, 201–224.
- Shimizu, Y.; Uemura, K.; Matsuda, H.; Miura, N.; Yamazoe, N. *J. Electrochem. Soc.* **1990**, *137*, 3430–3433.
- Prakash, J.; Joachin, H. *Electrochim. Acta* **2000**, *45*, 2289–2296.
- Vanderputten, A.; Elzing, A.; Visscher, W.; Barendrecht, E. *J. Electroanal. Chem.* **1986**, *205*, 233–244.
- Vanderputten, A.; Elzing, A.; Visscher, W.; Barendrecht, E. *J. Chem. Soc., Chem. Commun.* **1986**, 477–479.
- Wiesener, K. *Electrochim. Acta* **1986**, *31*, 1073–1078.
- Gupta, S.; Tryk, D.; Bae, I.; Aldred, W.; Yeager, E. *J. Appl. Electrochem.* **1989**, *19*, 19–27.
- Wei, G.; Wainright, J. S.; Savinell, R. F. *J. New Mater. Electrochem. Systems* **2000**, *3*, 121–129.
- Bouwkamp-Wijnoltz, A. L.; Visscher, W.; van Veen, J. A. R.; Tang, S. C. *Electrochim. Acta* **1999**, *45*, 379–386.
- Sawai, K.; Uda, D. *Chem. Lett.* **2006**, *35*, 1166–1167.
- Sawai, K.; Uda, D.; Shirai, K. *Electrochemistry* **2007**, *75*, 163–165.
- Toda, T.; Igarashi, H.; Uchida, H.; Watanabe, M. *J. Electrochem. Soc.* **1999**, *146*, 3750–3756.
- Stamenkovic, V.; Schmidt, T. J.; Ross, P. N.; Markovic, N. M. *J. Phys. Chem. B* **2002**, *106*, 11970–11979.
- Paulus, U. A.; Wokaun, A.; Scherer, G. G.; Schmidt, T. J.; Stamenkovic, V.; Radmilovic, V.; Markovic, N. M.; Ross, P. N. *J. Phys. Chem. B* **2002**, *106*, 4181–4191.
- Paulus, U. A.; Wokaun, A.; Scherer, G. G.; Schmidt, T. J.; Stamenkovic, V.; Markovic, N. M.; Ross, P. N. *Electrochim. Acta* **2002**, *47*, 3787–3798.
- Stamenkovic, V.; Schmidt, T. J.; Ross, P. N.; Markovic, N. M. *J. Electroanal. Chem.* **2003**, *554*, 191–199.
- Tamizhmani, G.; Capuano, G. A. *J. Electrochem. Soc.* **1994**, *141*, 968–975.
- Colmati, F.; Antolini, E.; Gonzalez, E. R. *J. Power Sources* **2006**, *157*, 98–103.
- Beard, B. C.; Ross, P. N. *J. Electrochem. Soc.* **1986**, *133*, 1839–1845.
- Stamenkovic, V. R.; Mun, B. S.; Arenz, M.; Mayrhofer, K. J. J.; Lucas, C. A.; Wang, G. F.; Ross, P. N.; Markovic, N. M. *Nat. Mater.* **2007**, *6*, 241–247.
- Yang, H.; Vogel, W.; Lamy, C.; Alonso-Vante, N. *J. Phys. Chem. B* **2004**, *108*, 11024–11034.
- Min, M. K.; Cho, J. H.; Cho, K. W.; Kim, H. *Electrochim. Acta* **2000**, *45*, 4211–4217.
- Zhang, J.; Lima, F. H. B.; Shao, M. H.; Sasaki, K.; Wang, J. X.; Hanson, J.; Adzic, R. R. *J. Phys. Chem. B* **2005**, *109*, 22701–22704.
- Camara, G. A.; Ticianelli, E. A.; Mukerjee, S.; Lee, S. J.; McBreen, J. *J. Electrochem. Soc.* **2002**, *149*, A748–A753.
- Jalan, V.; Taylor, E. J. *J. Electrochem. Soc.* **1983**, *130*, 2299–2301.
- Yeager, E. *Electrochim. Acta* **1984**, *29*, 1527–1537.
- Anderson, A. B.; Roques, J.; Mukerjee, S.; Murthi, V. S.; Markovic, N. M.; Stamenkovic, V. *J. Phys. Chem. B* **2005**, *109*, 1198–1203.
- Zhang, J. L.; Vukmirovic, M. B.; Sasaki, K.; Nilekar, A. U.; Mavrikakis, M.; Adzic, R. R. *J. Am. Chem. Soc.* **2005**, *127*, 12480–12481.
- Xu, Y.; Ruban, A. V.; Mavrikakis, M. *J. Am. Chem. Soc.* **2004**, *126*, 4717–4725.
- Wang, Y. X.; Balbuena, P. B. *J. Phys. Chem. B* **2005**, *109*, 18902–18906.
- Norskov, J. K.; Rossmeisl, J.; Logadottir, A.; Lindqvist, L.; Kitchin, J. R.; Bligaard, T.; Jonsson, H. *J. Phys. Chem. B* **2004**, *108*, 17886–17892.

- (43) Balbuena, P. B.; Altomare, D.; Vadlamani, N.; Bingi, S.; Agapito, L. A.; Seminario, J. M. *J. Phys. Chem. A* **2004**, *108*, 6378–6384.
- (44) Murthi, V. S.; Urian, R. C.; Mukerjee, S. *J. Phys. Chem. B* **2004**, *108*, 11011–11023.
- (45) Hwang, J. T.; Chung, J. S. *Electrochim. Acta* **1993**, *38*, 2715–2723.
- (46) Stamenkovic, V. R.; Mun, B. S.; Mayrhofer, K. J. J.; Ross, P. N.; Markovic, N. M. *J. Am. Chem. Soc.* **2006**, *128*, 8813–8819.
- (47) Tian, N.; Zhou, Z.-Y.; Sun, S.-G.; Ding, Y.; Wang, Z. L. *Science* **2007**, *316*, 732–735.
- (48) Poirier, J. A.; Stoner, G. E. *J. Electrochem. Soc.* **1994**, *141*, 425–430.
- (49) Takasu, Y.; Ohashi, N.; Zhang, X. G.; Murakami, Y.; Minagawa, H.; Sato, S.; Yahikozawa, K. *Electrochim. Acta* **1996**, *41*, 2595–2600.
- (50) Peuckert, M.; Yoneda, T.; Betta, R. A. D.; Boudart, M. *J. Electrochem. Soc.* **1986**, *133*, 944–947.
- (51) Sun, S. H.; Murray, C. B.; Weller, D.; Folks, L.; Moser, A. *Science* **2000**, *287*, 1989–1992.
- (52) Chen, W.; Kim, J.; Sun, S. H.; Chen, S. W. *Phys. Chem. Chem. Phys.* **2006**, *8*, 2779–2786.
- (53) Chen, W.; Kim, J. M.; Sun, S. H.; Chen, S. W. *Langmuir* **2007**, *23*, 11303–11310.
- (54) Chen, W.; Kim, J.; Xu, L.-P.; Sun, S.; Chen, S. W. *J. Phys. Chem. C* **2007**, *111*, 13452–13459.
- (55) Chen, W.; Sun, S. G.; Zhou, Z. Y.; Chen, S. P. *J. Phys. Chem. B* **2003**, *107*, 9808–9812.
- (56) Seidel, Y. E.; Lindstrom, R.; Jusys, Z.; Cai, J.; Wiedwald, U.; Ziemann, P.; Behm, R. J. *Langmuir* **2007**, *23*, 5795–5801.
- (57) Watanabe, M.; Tsurumi, K.; Mizukami, T.; Nakamura, T.; Stonehart, P. *J. Electrochem. Soc.* **1994**, *141*, 2659–2668.
- (58) Igarashi, H.; Fujino, T.; Zhu, Y. M.; Uchida, H.; Watanabe, M. *Phys. Chem. Chem. Phys.* **2001**, *3*, 306–314.
- (59) Bardi, U.; Beard, B. C.; Ross, P. N. *J. Catal.* **1990**, *124*, 22–29.
- (60) Bardi, U.; Atrei, A.; Zanazzi, E.; Rovida, G.; Ross, P. N. *Vacuum* **1990**, *41*, 437–440.
- (61) Ye, H. C.; Crooks, R. M. *J. Am. Chem. Soc.* **2007**, *129*, 3627–3633.
- (62) Kumar, S.; Zou, S. Z. *Electrochem. Commun.* **2006**, *8*, 1151–1157.
- (63) Markovic, N.; Gasteiger, H.; Ross, P. N. *J. Electrochem. Soc.* **1997**, *144*, 1591–1597.
- (64) Schumpe, A.; Adler, I.; Deckwer, W. D. *Biotechnol. Bioeng.* **1978**, *20*, 145–150.
- (65) Anastasijevic, N. A.; Dimitrijevic, Z. M.; Adzic, R. R. *Electrochim. Acta* **1986**, *31*, 1125–1130.
- (66) Markovic, N. M.; Gasteiger, H. A.; Grgur, B. N.; Ross, P. N. *J. Electroanal. Chem.* **1999**, *467*, 157–163.
- (67) Huang, J.-S.; Zhang, X.-G.; Luo, J.-M.; Sun, Y.; Yang, J. *J. Solid State Electrochem.* **2007**, in press.
- (68) Vaik, K.; Sarapuu, A.; Tammeveski, K.; Mirkhalaf, F.; Schiffrin, D. J. *J. Electroanal. Chem.* **2004**, *564*, 159–166.
- (69) Sarapuu, A.; Vaik, K.; Schiffrin, D. J.; Tammeveski, K. *J. Electroanal. Chem.* **2003**, *541*, 23–29.